Dynamic cracking process of rock interpreted by localized strain-rate, rate-dependent strength field and transition strain-rate

Chunjiang Zou [a], Jianchun Li [b], Kai Liu [c,*], Xiaobao Zhao [d]

[a] Department of Civil Engineering, Monash University, Australia
[b] School of Civil Engineering, Southeast University, China
[c] Department of Engineering Science, University of Oxford, United Kingdom
[d] School of Earth Sciences and Engineering, Nanjing University, China

A B S T R A C T

The cracking mode of rock under dynamic loadings is significantly different from that under quasi-static loadings. One of the underlying mechanisms is the variation of the rate-dependent mechanical properties under different loading rates. However, the rate-dependent mechanical properties cannot explain the transition of the failure mode and the suppression of the tensile cracks under dynamic loading. In this paper, the interaction between the rate-dependent properties and the geometrical effect of pre-existing flaws is investigated and successfully explained these questions. The classical single-flaw model providing a good stress concentration at possible crack initiation positions and material homogeneity is used to analyse the stress, strain, strain rate, and rate-dependent strength fields experimentally and mathematically. The rate-dependent strength field in the dynamic regime is proposed and seen as the key to the cracking mode change. Based on the dynamic tests on intact specimens, the tensile strength is generally found more sensitive to strain rate than the compressive strength. Due to the uneven strain induced by stress concentration around the flaw, the strain rate is also uneven and proportional to the stress intensity naming the "localized strain rate effect". In the analytical study, the equations of the "transition strain rate" as a watershed for the different fracturing behaviours are given. The theoretical study shows that the dynamic mechanical properties and the geometry-induced stress/strain rate distribution non-uniformity should be coupled together to analyse the failure process of rocks.

1. Introduction

The rocks or brittle rock-like materials have different cracking patterns when loaded under different rates, according to practical observations. For example, blasting on rocks in underground engineering or mining activities usually produces significantly more cracks, including both large size, small size and microscopic radial cracks as well as some circular cracks, while hydraulic fracturing only produces very few radial cracks. Not only in the engineering region, geological processes, like earthquakes and meteorite impacts, involve very high-rate loadings ranging typically from 10 to 10^4 s^{-1} or even higher,[1–5,5–34] also have different failure modes compared with the quasi-static or creeping distortion.

Rock masses are not intact but contain inherent defects such as flaws, fractures, joints, caves or faults. In the mesoscopic and microscopic views, a rock material is also not intact. It contains a large number of randomly oriented zones of potential failure in the form of voids and grain boundaries. Such defects induce very high stress concentration due to the geometry effect. Cracks will initiate and develop around these defects. The present study establishes a simplified model to investigate the loading rate effects on the crack initiation and failure mode. In the quasi-static regime, the crack initiation and propagation of rocks with pre-existing artificial flaws have been comprehensively studied,[6–14] and such investigation on the rock with pre-existing flaws in the dynamic regime has increased recently,[15–20] rather than the investigation on the fragmentation[2,3,21] and the spalling phenomena.[22] However, most of the dynamic research concentrates the experimental observation. The theoretical analyses of the different fracturing behaviour are still needed to explain the mechanism behind the experimental results.

The geometry effect is not the only dominant factor. Most of the mechanical properties of materials like wood, ice, concrete, soft materials, rocks and foams, also vary with the strain rate. The strain rate can

---

* Corresponding author.
  E-mail address: kai.liu@eng.ox.ac.uk (K. Liu).

also affect the cracking behaviour, according to the Griffith or other fracture theories. The influences of the strain rate on various mechanical properties of rocks, e.g. strength, fracture toughness and elastic modulus, are studied by different laboratory methods such as drop weight test,[23,24] impact test,[25,26] split Hopkinson pressure bar (SHPB) test[27–35] and other dynamic techniques.[36,37] However, the definition of 'high strain rate' in engineering is different from the definition in tectonics which is still in the quasi-static or creeping region.[38] In these studies, the tensile and compressive strength,[28,39,40] the shear strength[41] and the three modes of fracture toughness[42,43] of rocks or rock-like materials all illustrated obvious rate-dependence on different levels.

Due to the better accessibility of the strength of rocks than the three types of fracture toughness under dynamic loadings, the concept of local failure of small elements to represent crack initiation, and the connection of these failed elements to represent the propagation of a macroscopic crack, is introduced in the present study. The analysis method is named the 'micro-element method' in this study. The interactions between the rate-dependent mechanical properties of rocks and the rate-dependent cracking behaviour are investigated through the single-flawed marble specimens. The existence of the flaw leads to the stress concentration and hence induces different strains at different positions around the flaw. When the load is dynamic, such differences in strain value cannot be neglected. This phenomenon induces the localized strain and eventually produces the localized strain rate. The strain rate will also affect the dynamic strength, resulting in the variation of micro-elements' dynamic strength, which brings in the concept of the rate-dependent strength field. Since the increase rate of the tensile strength is faster than that of the compressive strength, the initiation of the tensile crack could be potentially suppressed, causing the transition of crack initiation mode. Therefore, three new concepts, which are the 'localized strain rate', the 'rate-dependent strength field' and the 'transition strain rate', are proposed in the present study to explain the
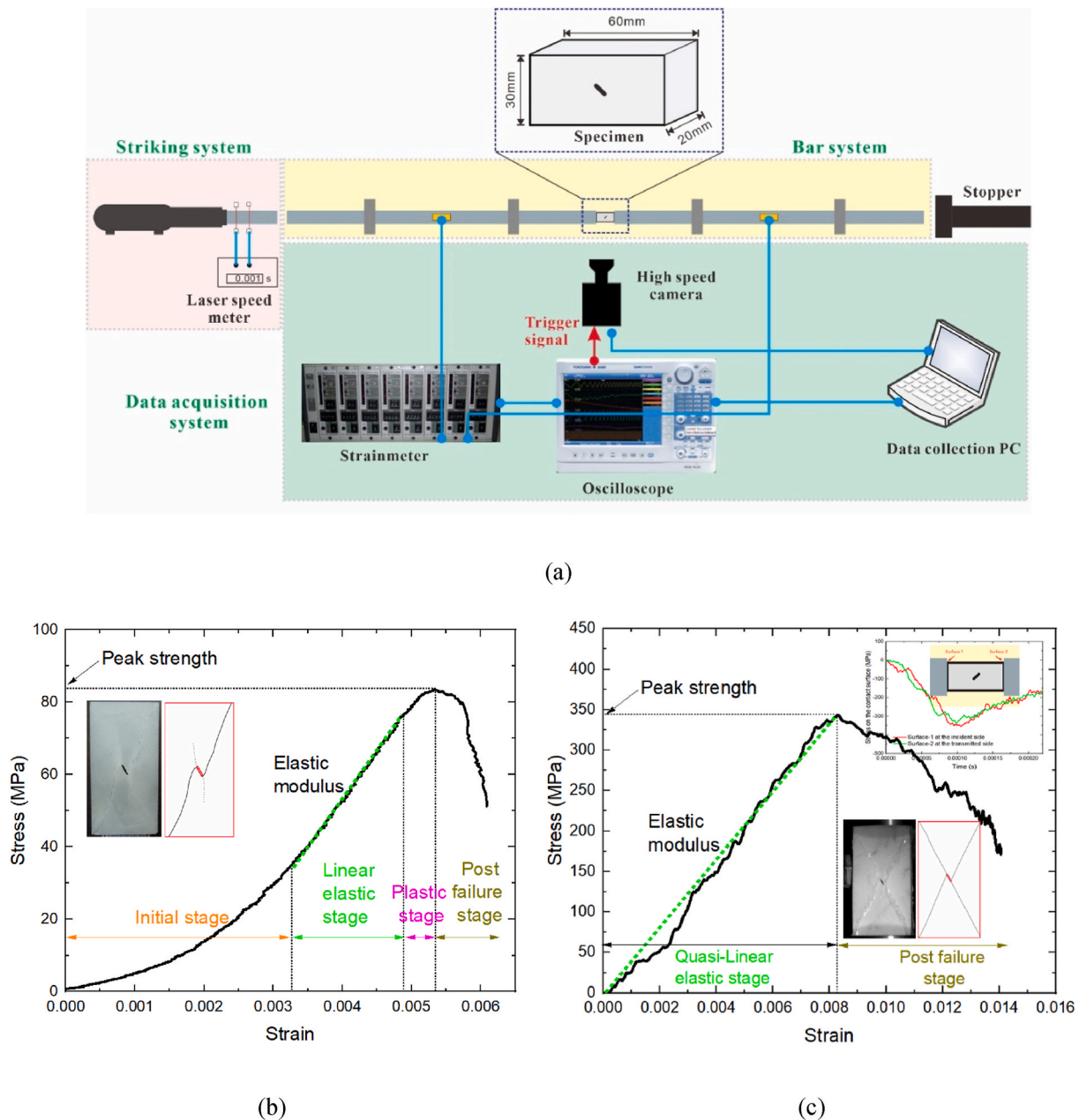

(a)

(b)

(c)

Fig. 1. (a) Setup of the SHPB testing system; (b) Typical strain-stress curve and failure mode of a single-flawed marble with the inclination angle of 30° under a quasi-static loading; (c) Typical strain-stress curve, force equilibrium state and failure mode of the same single-flawed specimen under a dynamic loading.

experimental rate-dependent fracturing phenomena theoretically.

2. Material and methods

2.1. Material and specimens

The Carrara marble with the low intrinsic crack density, even grain distribution and low porosity is utilized to fabricate the single-flawed specimen considering the repeatability of experimental results. The cracking process of marble usually experiences two stages: white patches[20,44,45] and macroscopic cracks.[20] Previous studies indicate that the initiation of white patches shares the same trajectories with the further macroscopic cracks (macro-cracks), while it is noted that some white patches will not evolve further to the macro-cracks. The white patch helps track the potential stress concentration and the crack initiation point easier. The geometry of the specimens used for this study is shown in Fig. 1. The single-flawed prismatic specimens are fabricated by an abrasive jet cutter which can provide a cutting width of less than 0.5 mm. The single-flawed specimens have different inclination angles, which are defined as the angle between the maximum force and the longer axis of the flaw, to investigate the influence of the load direction on the cracking behaviour.

2.2. Loading conditions

The split Hopkinson pressure bar (SHPB), which can provide a strain rate up to 10^3 s^{-1}, is used to perform dynamic compressive and Brazilian tensile tests as well as the cracking tests on the single-flawed marble. Pulse shapers are placed to produce a smooth and gentle incident wave and hence a relatively stable strain rate. All the specimens have achieved the force equilibrium state which is checked by both the experimental result and the theoretical maximum allowable strain rate applied on the specimen with a certain length given by Ravichandran and Subhash (1994).[46] The maximum allowable strain rate for the 60 mm long specimen is determined to be 250 s^{-1} in the SHPB test. To obtain the variation of strength and cracking behaviour in the quasi-static regime, a servo-hydraulic loading machine is conducted using the displacement control mode (0.001 mm/s). High-speed video is applied in every test with a frame rate of 40,000 fps. The average longitudinal wave speed V_p of Carrara marble is about 5936 m/s. Since the cracking speed is usually less than the shear wave speed (about 3000 m/s) and the actual crack speed is generally much less than this value, from several hundreds to 1000 m/s,[47–50] the crack will propagate only a few millimetres to several centimetres between two frames, this frame rate is enough to capture the cracking details and sequencing based on the cracking speed and specimen dimensions. The actual high-speed videos about the failure process also confirmed this capability. The setup is shown in Fig. 1. In data processing, data is processed as raw as possible with limited filtering and revision to strengthen the data reliability.

3. Experimental results

3.1. Compressive and tensile DIFs

The dynamic increase factor (DIF), the ratio of the dynamic strength and the average quasi-static strength, is introduced to depict the increment degree of strength with strain rate. The TDIF and CDIF represent the DIFs for tensile and compressive strength, respectively. The variation of TDIF and CDIF of the Carrara marble with the strain rate is shown in Fig. 2, which has been reported by the authors' previous papers.[19,20,45] The fast increase of the DIFs indicates obvious rate-dependence of both tensile and compressive strength in the dynamic regime. The rising speed of dynamic tensile strength is about 2.5 times the compressive strength reflected by the ratio between the TDIF and CDIF. Based on the empirical equations given in the literature,[26,51] the logarithmic equations fit well with the data, as illustrated in Eq. (1)
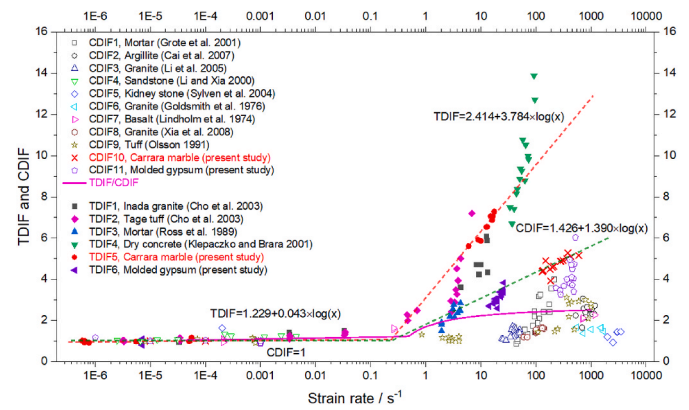

Fig. 2. Compressive and tensile DIFs of Carrara marble under various strain rates and the corresponding fitting curves compared with the TDIF/CDIF of various brittle materials compiled from the literatures.[19,32,45,52–62,73]

and Eq. (2). Due to the difficulty in producing the semi-dynamic strain rates from 10^{-3} to 1 s^{-1}, there is a gap in testing data. The elongations of the quasi-static fitting line and the dynamic fitting line are used to cover this gap. The result indicates that the tensile strength is more sensitive to the strain rate, and the hardening of tensile strength is more prominent, which may raise the difficulty of tensile crack initiation and even induce the suppression of the tensile cracks. Similar results were reported for many rock types in literature like granite, tuff, mortar, concrete, sandstone, basalt, argillite et al.,[19,32,45,52–73] as shown in Fig. 2. Therefore, the findings in the present study can be applied to analyse the dynamic cracking process of other rock types.

$$CDIF = 1.426 + 1.390\ log\dot{\varepsilon}\ \ for\ 0.5\ s^{-1} \leq \dot{\varepsilon} \leq 600\ s^{-1}\ \ CDIF = 1\ for\ \dot{\varepsilon}$$
$$< 0.5\ s^{-1}$$

<div align="right">Eq. 1</div>

$$TDIF = 2.414 + 3.784\ log\dot{\varepsilon}\ \ \ for\ 0.5\ s^{-1} \leq \dot{\varepsilon} \leq 600\ s^{-1}\ TDIF$$
$$= 1.229 + 0.043\ log\dot{\varepsilon}\ for\ \dot{\varepsilon} < 0.5\ s^{-1}$$

<div align="right">Eq. 2</div>

3.2. Fracturing processes of single-flawed marble

3.2.1. Stress around the flaw

The stresses around a single flaw with different inclination angles are illustrated in Fig. 3, given by the finite element simulation with very fine elements. Three types of stress states based on the stress vectors in the two-dimensional model are classified in Fig. 4. If the principal stresses σ_1 and σ_3 of an element are both tensile, the element is under pure tension. The assembly of these elements is defined as the pure tension zone. Similarly, the assembly of those elements with the compressive principal stresses is defined as the shear failure zone/pure compression zone. If one of the principal stresses is tensile and another one is compressive, the element can fail either under tensile mode or under shear mode. Therefore, the assembly of these elements is defined as the mixed tension and compression zone. The pure tension zone, the mixed tension-compression zone (abbreviated 'the mixed zone') and the pure compression zone are marked by red, yellow and blue, respectively, as presented in Fig. 3. The analysis based on the Mohr-Coulomb criterion for these stress states is also shown in Fig. 4.

The failure mode for the elements in the mixed tension-compression zone can gestate both tensile and shear failure judged by the stress state and the failure envelope. According to Fig. 3, the pure compression and tension zones dominate the elements around the flaw boundary, coincident with the theoretical analysis. The pure tension zone dominates the flaw boundary when the inclination angle is high and decreases fast with the inclination angle. It occupies an inconspicuous region that can be neglected when the inclination angle is 0°. In contrast, the pure
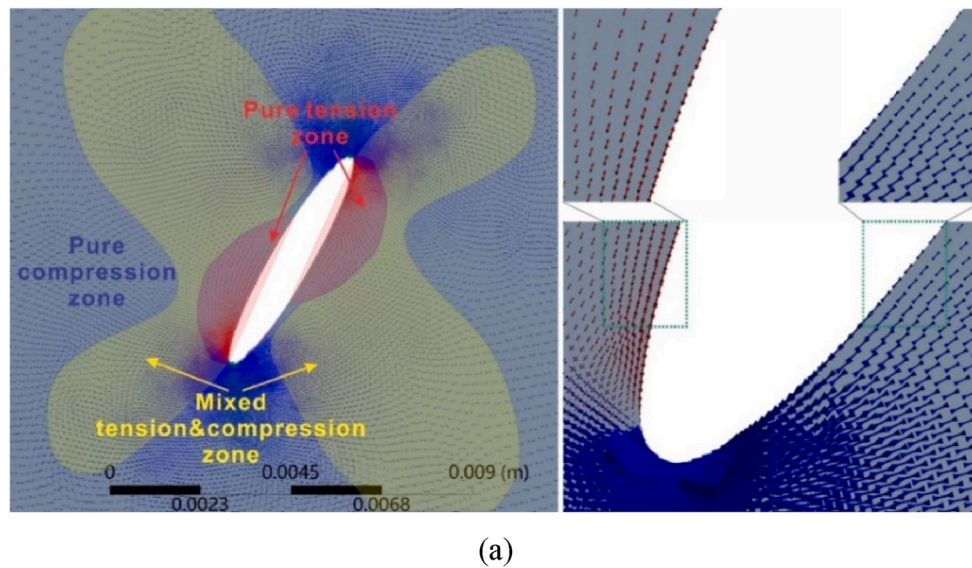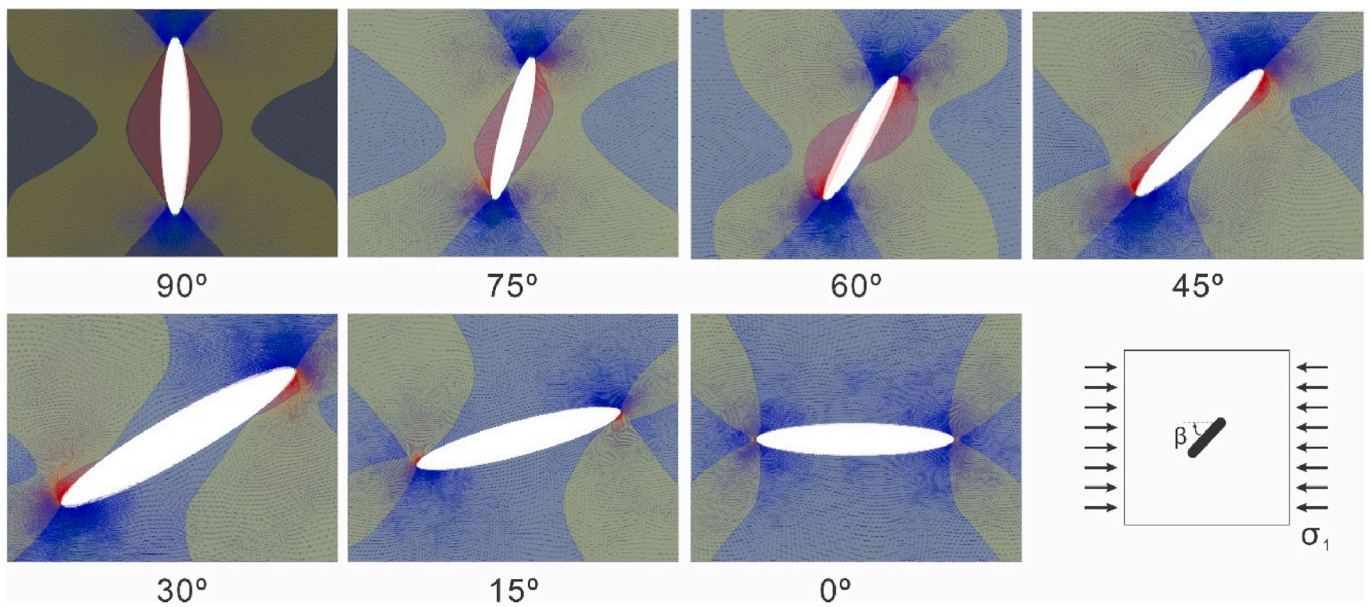
(a)

Fig. 3. (a) Tension zone, mixed tension-compression zone and compression zones (other places) around the elliptical flaw with the inclination angle of 60° and (b) the variation of these zones with the inclination angle from 0° to 90°.

compression zone replaces the space given by the pure tension zone. The existence of the mixed zone explains the tensile property of the wing cracks and the anti-wing cracks in the quasi-static loading conditions (observed by Wong 2008 [63]) due to much lower tensile strength compared with compressive strength for rocks, and the tip of the anti-wing cracks might initiate at the mixed zone or the shear zone.

3.2.2. White patch development

There are two stages of the fracturing process, which are white patch development and macro-crack development. Previous studies revealed that the loading rate does not affect the initiation point of the white patches but can affect the crack initiation, propagation and failure mode of marble.[20] The appearance of white patches much earlier for the stress-strain curve before macro-cracks despite the loading rate (Fig. 5a, b). A pixel comparison code is used to enhance the white patches with black dots in the figure. According to the definition of white patch types,[20] the area of the tensile white patches is significantly smaller than the shear, which is understandable because of the very limited pure tension area for this model, as shown in Fig. 3. The shear patches increase accordingly with the load, while the tensile patches show no

significant development, which indicates that the shear deformation can produce more white patches.

3.2.3. Cracking process

The crack initiation under dynamic loadings is completely different from that under quasi-static loadings, though the initiated white patches are not affected by the loading rate. Under dynamic loadings, the crack initiation points appear as two pairs (shear cracks) simultaneously, or one pair appears (shear cracks) closely following another pair (anti-wing cracks) in an extremely rapid sequence.[20] No tensile wing patches will develop into any visible macro-cracks. Moreover, according to the stress state of the initiation point by the FEM modelling, the crack initiation point around the flaw under quasi-static conditions is at the tensile zone, while the initiation point under dynamic conditions is at the compression zone, which represents the shear cracks. The tensile cracks are suppressed under dynamic loadings.

As shown in Fig. 5, there are two types of failure patterns under quasi-static loadings[20]: the visible cracks marked by blue lines and the failure patterns without visible cracks marked by semi-transparent blue lines. The failure patterns without visible cracks correspond to the
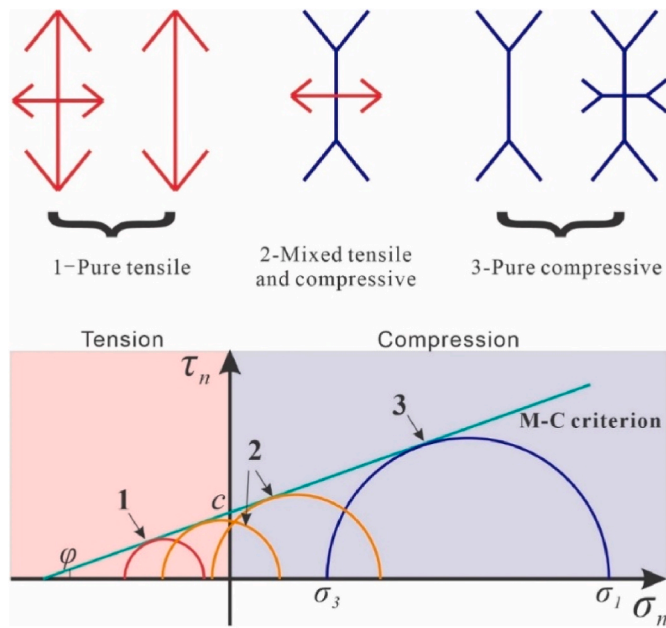
Fig. 4. Stress vectors of the elements and the corresponding failure modes.

early-initiated tensile or shear patches which are suppressed in the process of loading increment. Tensile cracks or failure patterns are the first to be observed by a high-speed camera. However, they are also

one-dimensional for the elements along the flaw boundary, the principal stress can be regarded as the tangential stress. It is found that the distributions of tangential stress of these two flaws are very similar. When the tangential stress is larger than zero, it is tensile; conversely, it is compressive. The only significant difference is that the elliptical flaw induces higher stress concentration in the narrow areas around the sharp tips. The maximum compressive stress around the straight flaw is about half of that around the elliptical flaw. However, the maximum tensile stresses are similar to each other. Since the tensile strength of a brittle material like rock is extremely lower than the compressive strength, the tensile failure dominates the crack initiation. Therefore, the application of the elliptical flaw model can reflect the stress variation in the round-tip straight flaw model, though the estimated compressive failure might be slightly over-estimated. The analysis and phenomenon obtained based on the elliptical flaw model are reliable.

4.2. Tangential stress around an elliptical flaw

The tangential stress around an elliptical flaw had been given by previous literature[64] based on two assumptions to simplify the question: (a) the space around the only flaw is infinite, or the adjacent flaws are far away enough so the interactions can be ignored; (b) two-dimensional stress state while the stress normal to the plane is zero ($\sigma_2 = 0$). The magnitude of the error introduced by these two assumptions was estimated to be less than 10%.[64] As the detailed deduction has been given by Hoek,[64] the present study provides the key equations about the solutions to stresses, including the tangential stress around the flaw (Eq. (3)). The coordinate and flaw system are shown in Fig. 7.

$$\sigma_b = \frac{1}{m^2\cos^2\alpha + \sin^2\alpha}\left\{\sigma_y\left\{m(m+2)\cos^2\alpha - \sin^2\alpha\right\} + \sigma_x\left\{(1+2m)\sin^2\alpha - m^2\cos^2\alpha\right\} - \tau_{xy}\left\{2(1+m^2)\sin\alpha\cos\alpha\right\}\right\} \qquad \text{Eq. 3}$$

suppressed in the following compression due to the dominant compressive stress state in all types of specimens. The visible anti-wing cracks appearing as a pair lead to the diagonal failure mode. Therefore, it can be concluded that tensile cracks dominate the early stage of cracking, while shear cracks dominate the following failure stage under quasi-static loading conditions.

4. Data analysis

As stated in previous sections, the variation of mechanical properties with the strain rate affect distinctively the crack behaviour. The influencing mechanism of the rate-dependent strength on the crack mode is discussed in this section. The analytical solution of tangential stress around an elliptical flaw[64] is used for the analysis.

### 4.1. Round-tip straight flaw VS elliptical flaw

In the experimental study, due to the limitation of the fabrication technique, the flaw is straight with two perfect round tips. In contrast, in the theoretical analysis, the flaw is a perfect ellipse. However, the analytical solution of the tangential stress around a round-tip straight flaw is hard to obtain. Fortunately, the analytical solution for the elliptical flaw has been given in the literature.[64] The theoretical analysis will be more practical if the problem can be simplified as an elliptical flaw. Here, the influence of the flaw shape on the stress distribution around the flaws is discussed using finite element analysis.

Fig. 6 illustrates the numerical results of the principal stress distribution (i.e. normalized tangential stress) around these two types of flaws under 1 MPa uniaxial compression.[65] Since the stress state is nearly

where α is the eccentric angle; $m = b/a$ is the ratio of the minor to the major axis length of the ellipse; β is the inclination angle between the loading direction of σ_1 and the long axis of the elliptical flaw; σ_b is the tangential stress on the ellipse boundary. When $\sigma_b < 0$, the stress is tensile and denoted by σ_{bt}; when $\sigma_b > 0$, the stress is compressive and denoted by σ_{bc}. The flatness of cracks or defects in brittle material like rocks could be very high. In other words, the coefficient m is usually assumed as very small.

The tangential stress distribution around an ellipse is illustrated in Figs. 8 and 9, based on the results of finite element simulation with very fine meshing and coincident with the result given by Eq. (3). When the flaw's inclination angle increases, the tension zone and the peak compressive stress decrease gradually. Interestingly, the variation of the peak tensile stress is not monotone. The maximum tensile and compressive strength are shown in Fig. 10 and Table 1. The inclination angles of 45° and 60° exhibit the highest tensile stress concentration. As the compressive strength is several times the tensile strength for most of the brittle rocks (e.g. granite, marble, sandstone, etc.), tensile cracks will occur first during the loading. In Fig. 10, the normalized stress/strength, which is the ratio of the maximum stress (tensile or compressive) to the corresponding strength, is the key factor in depicting the micro-element state: (1) when it is less than one, the element is stable and at the 'safe zone'; (2) when it is over one, the element is not stable and at the 'cracking zone'.
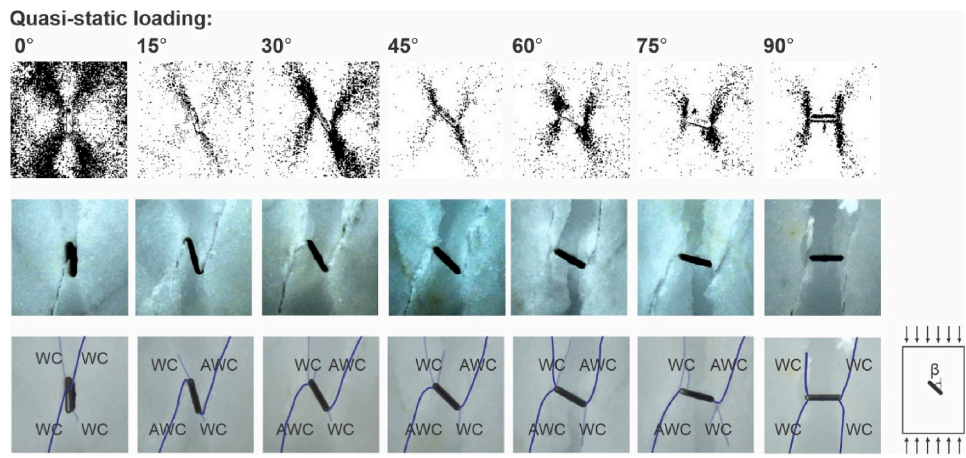
For Carrara marble, since the ratio of the normalized compressive stress to the corresponding compressive strength is always lower than one (safe zone), while the ratio of the normalized tensile stress to the corresponding tensile strength is larger than one (cracking zone), the tensile wing cracks always occur first, as given by Table 1. In other
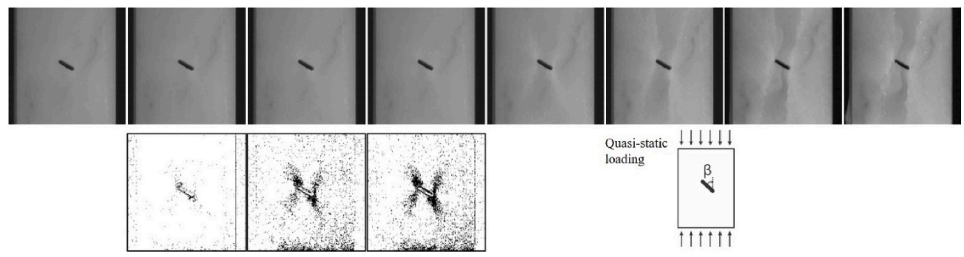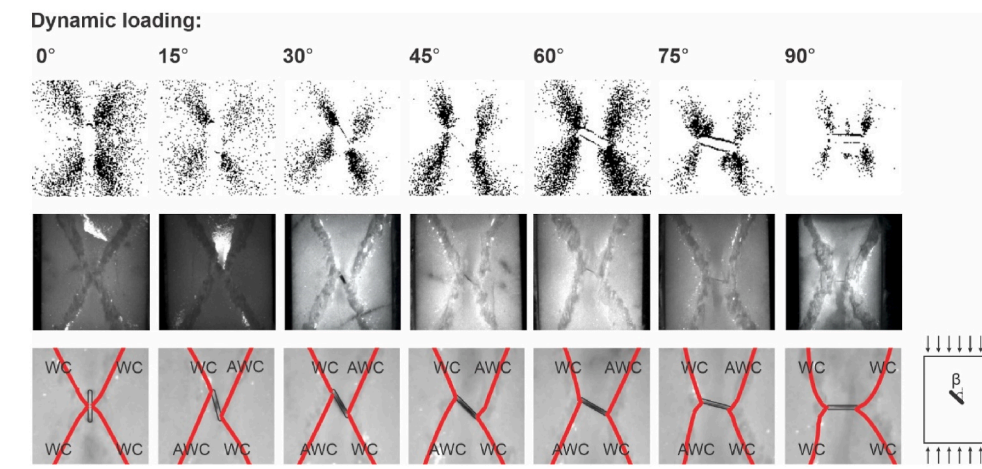
(a)
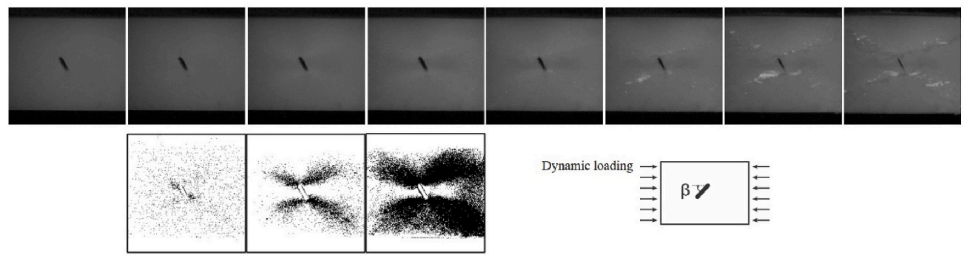
(b)

(c)

(d)

Fig. 5. Cracking processes of two typical single-flawed marble specimens with the inclination angle of 60° under quasi-static (a) and dynamic (b) loadings, and the comparison of the white patch initiation, crack pattern and failure modes with various inclination angles under quasi-static (c) and dynamic (d) loadings.[20]
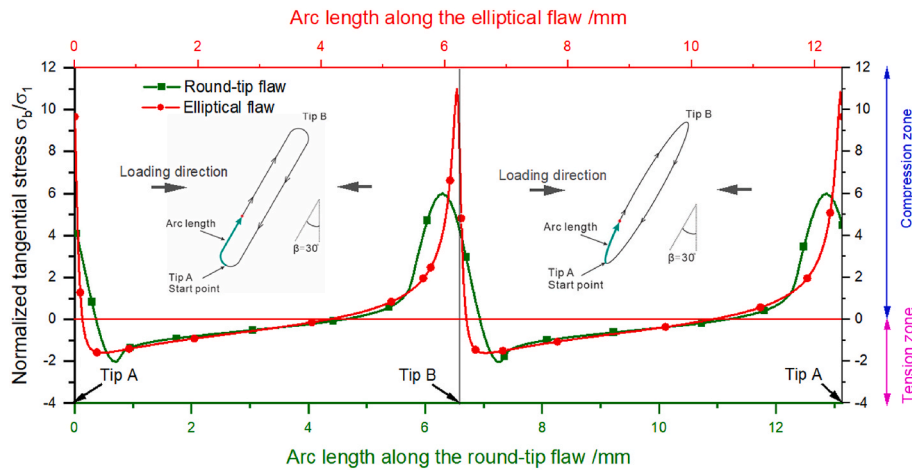
Fig. 6. Comparison of normalized tangential stress along with two different types of flaws with the inclination angle of 60°[65].
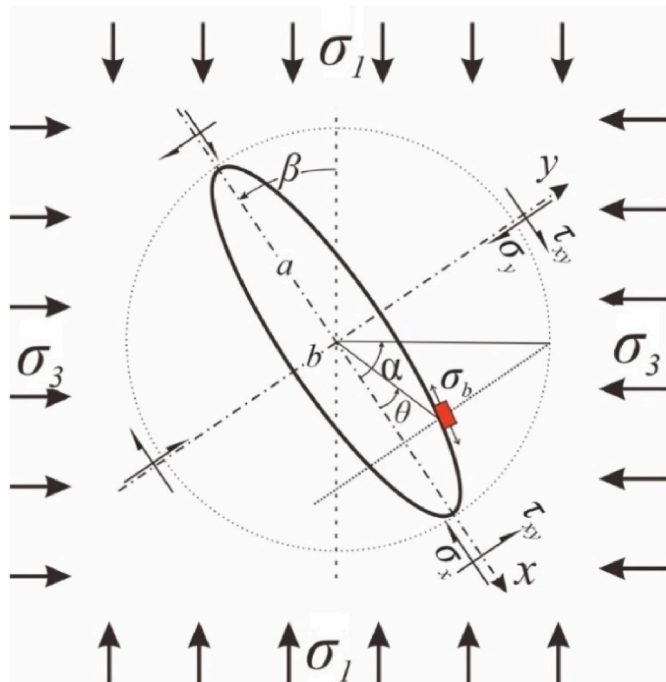

Fig. 7. Stress system acting on an elliptical open flaw.

words, for a quasi-static load with a constant loading rate, the tensile crack generally occurs first. The corresponding applied force is lowest for specimens with the inclination angle of 45° and 60°. Such theoretical analysis well explains the experimental findings.[66]

4.3. Micro-element method

Unlike the Griffith theory of fracture based on energy, this study uses the concept of 'micro-element' to depict the mechanical state of microscopic rock elements. In the 'micro-element method', the early-stage failure of the micro-element causes the initiation of new cracks, while the following failure of more micro-elements leads to the propagation of the initiated cracks or the developing of new cracks. The failure of the micro-element is dependent on the stress state. Generally speaking, the failure can have two types: tensile and compressive failure, corresponding to the tensile and shear crack. Using the micro-element method will make it easier to understand the crack type intuitively and link the macroscopic mechanical properties to the cracking process.

In addition, for those model who do not have analytical solutions for the stress around the flaw boundary, this method can be used with the FEM simulation to deal with the flawed specimens with complicated geometries. By updating the FEM model, the crack trace can also be obtained for these complicated specimens or application conditions.

In Fig. 7, the normal stress of the micro-elements at the ellipse boundary is zero. The micro-elements are considered as the one-dimensional stress state. Hence, the maximum principal stress coincides with the tangential stress in the same direction, while the minimum principal stress is zero. It is noted that the tensile stress is negative, and the compressive stress is positive in the present study. When the stress is negative, and the absolute value exceeds the tensile strength, the micro-element will fail as a tensile mode. In contrast, when the stress is positive and exceeds the uniaxial compressive strength, the micro-element will fail in a compressive mode.

For the quasi-static loading conditions, the strength is considered uniform at any location for the analysis of failure in a homogeneous and intact material. When there are defects or flaws inside the material, the stress concentration and the induced strain concentration do exist. Theoretically, the strain rate around such defects is different. However, according to the experimental studies, the strain rate effect on the strength can be neglected under quasi-static loading conditions due to its insensitivity to strain rate. In other words, the strength of every micro-element is also uniform.

As stated in section 3.1, the strength of material changes with the applied loading rate or strain rate for the dynamic loading conditions or the high strain rate. As we know that the stress of the micro-elements inside material with defects or flaws is not identical, the stress concentration cannot be ignored. If the elastic modulus is constant with the strain rate, we can say that the strains of micro-elements are different, and the strain of the micro-elements with higher stress concentration is higher. Divided by time, the strain rates of micro-elements with stress concentration zone are also higher, as shown in Fig. 11. Here, we propose a new concept, *'strain rate field'*, in the dynamic regime. According to Fig. 11b, the range of the strain rate increase significantly with the applied axial strain rate $\dot{\varepsilon}_0$. When the applied axial strain rate is low, the influence of the strain rate variation can be neglected. But when the applied strain rate reaches the dynamic regime, such influence should be taken account. Therefore, considering the strain rate-dependent strength, the actual strengths of the micro-elements around the defects are different, which indicates the *'localized strain rate effect'*. Then, another new concept, *'strength field'*, is used to depict strength distribution in the dynamic mechanics. This concept is rarely discussed in previous studies on rock mechanics because most of them are quasi-static.

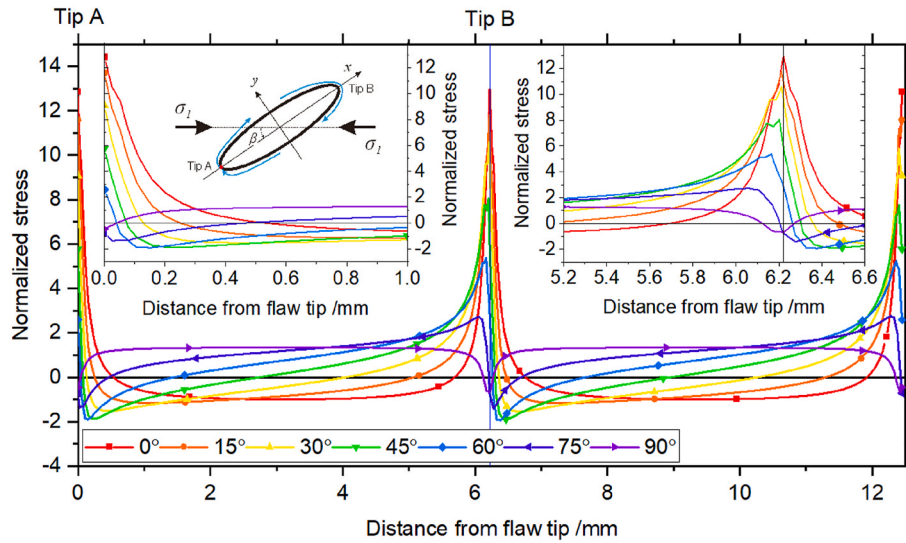The ratio of the elementary strength to the corresponding stress of

Fig. 8. Normalized principal stress along the boundary of an elliptical open flaw with different inclination angles based on numerical results (tensile-negative, compressive-positive).
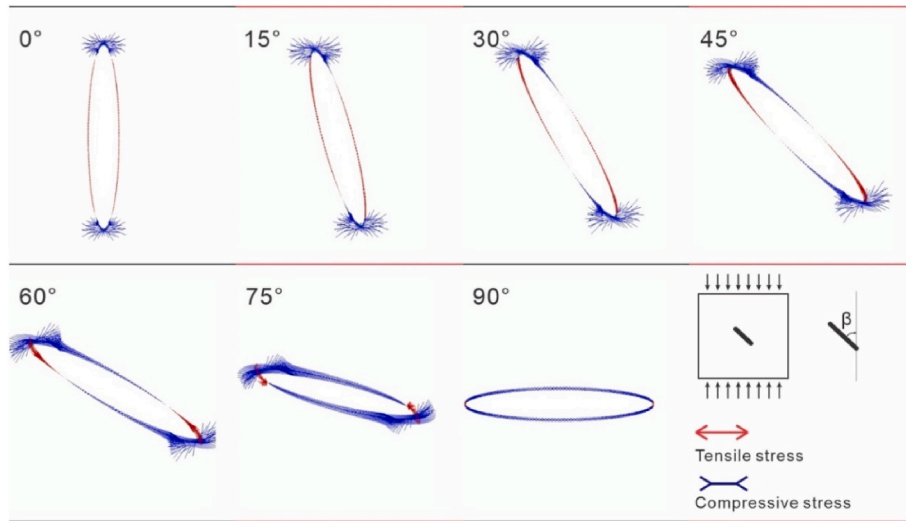

Fig. 9. Principal stress vector along the elliptical flaw boundary with different inclination angles.

the micro-elements along the flaw boundary is defined as the **'elementary safety factor λ'**. For the tensile stress state, the tensile safety factor λ_t is the ratio of tensile strength to tensile stress $\sigma_t / \sigma_{t-max}$, while the compressive safety factor λ_c is $\sigma_c / \sigma_{c-max}$. If the elementary safety factor λ is less than one, the corresponding microelement is unsafe and will fail immediately. Since the compressive strength is generally an order of magnitude higher than the tensile strength for brittle materials like rocks under quasi-static conditions, the λ_c is always higher than one before any element failure, so the tensile failure occurs typically. The point which has the maximum tensile stress is the crack initiation point.

However, the dynamic fracturing process is different. According to Fig. 12a, the dynamic tensile strength increases faster than the dynamic compressive strength. The dynamic compressive stress/strength ratio $\sigma_{c-max}/\sigma_{c-dyn}$ increases faster than the dynamic tensile stress/strength ratio $\sigma_{t-max}/\sigma_{t-dyn}$. Under a certain strain rate, the two ratios $\sigma_{c-max}/\sigma_{c-dyn}$ and $\sigma_{t-max}/\sigma_{t-dyn}$ will be equal. Alternatively, the dynamic λ_t and λ_c are equal to be one (Fig. 12b). After that, the compressive failure will occur first instead of the tensile failure. The point having the maximum compressive stress is the crack initiation point. Such a strain rate is defined as the **'transition strain rate'**. The present study is trying to

determine the analytical solution of the transition strain rate based on the analytical solution for the tangential stress around the flaw and the experimental results about the dynamic increase factors. The analysis process is the so-called **'micro-element method'** with the idea flow-chart shown in Fig. 13.

4.4. Tangential stress and crack initiation under quasi-static loadings

The inclination angle β of the pre-existing flaw significantly affects the stress distribution around the flaw. As shown in Fig. 14, the tangential stress is normalized by being divided by the applied uniaxial stress. A higher inclination angle results in higher maximum stress (compressive) but with little influence on the minimum stress (tensile). The positions of the extreme values also change with the inclination angle. With the increase of β, the maximum value moves to the flaw tips, while the minimum value moves to the flaw centre. Meanwhile, the compressive zone becomes more concentrated with the expansion of the tensile zone. Under quasi-static loadings, the determination of the crack initiation point is based on the comparison of maximum tensile stress and compressive stress with their corresponding strength, namely, the
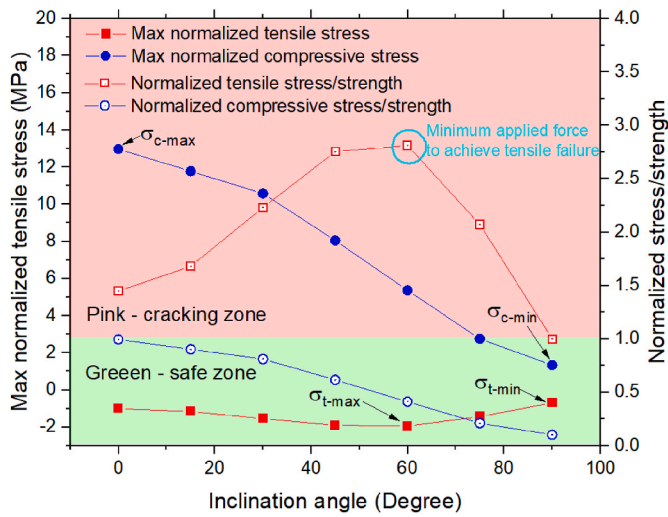
Fig. 10. Variation of tangential stress and the normalized stress/strength ratio to indicate the failure mode.

Table 1
(1) Maximum normalized tensile stress and normalized compressive stress along the boundary of the elliptical flaw with different inclination angles; (2) Stress/strength ratio for the tensile and compressive stress conditions (Carrara marble: compressive strength 90 MPa, tensile strength 6.9 MPa).

Inclination angle	0	15	30	45	60	75	90
Max normalized tensile stress/MPa	1.00	1.16	1.54	1.90	1.94	1.43	0.69
Max normalized compressive stress/MPa	-12.97	-11.78	-10.58	-8.05	-5.37	-2.76	-1.34
Normalized tensile stress/strength	1.00	1.16	1.54	1.90	1.94	1.43	0.69
Normalized compressive stress/strength	0.99	0.90	0.81	0.62	0.42	0.21	0.10

$\sigma_{t-max}/\sigma_{t-static}$ and the $\sigma_{c-max}/\sigma_{c-static}$ is larger than 1.

For the analytical model of a single elliptical flaw, the maximum tangential stress along the flaw boundary can be obtained when

$$\frac{d\sigma_b}{d\alpha} = 0 \qquad \text{Eq. 4}$$

Assuming that the flatness of a flaw is very high, meaning a very small axis ratio m, which is consistent with the natural cracks in rocks. In the last section, it is determined that the tensile crack generally initiates first. Hence, determining the position of the maximum tensile stress is to determine the crack initiation point around the flaw. According to Fig. 8, except for the case with a flaw inclination angle equal to 0°, the eccentric angle α at the maximum tensile stress point is with a small value. Hence, when $\alpha \to 0$, $\sin \alpha \to \alpha$ and $\cos \alpha \to 1$. Therefore, the terms of the second order or the higher order of $\sin \alpha$, m and their combination can be neglected to simplify the equation. The tangential stress equation Eq. (3) can be rewritten as Eq. (5) by substituting these simplifications:

$$\sigma_b = \frac{2(\sigma_y \bullet m - \tau_{xy} \bullet \alpha)}{m^2 + \alpha^2} \qquad \text{Eq. 5}$$

Substituting Eq. (5) to Eq. (4) gives

$$\sigma_b = \frac{-\tau_{xy}}{\alpha} \qquad \text{Eq. 6}$$

Or

$$\alpha = \frac{-\tau_{xy}}{\sigma_b} \qquad \text{Eq. 7}$$

The value of α corresponding to the maximum tangential tensile stress provides the position of the crack initiation point. From Eq. (5) and Eq. (6), the relationship between the maximum tensile stress σ_{bmax} and the external applied stress can be obtained

$$\sigma_{bmax} \bullet m = -\sigma_y \pm \sqrt{\sigma_y^2 + \tau_{xy}^2} \qquad \text{Eq. 8}$$

4.5. Tangential stress and crack initiation under dynamic loadings

Under dynamic loadings, the determination of the crack initiation point is different from that under quasi-static loadings due to the rate-dependent strength. Nonetheless, the dynamic stress/strength ratios $\sigma_{c-max}/\sigma_{c-dyn}$ and $\sigma_{t-max}/\sigma_{t-dyn}$ are still the criterion for crack initiation. As stated in the previous sections, due to the strain rate effect, the rate-dependent strength field and strain rate field of rock should be considered during the dynamic load. The stress, strain, strain rate and strength are localized and vary at different positions, especially around the flaw, due to the significant stress concentration.

A comparison between theoretical and simulated results is conducted to verify the validity of investigating the localized strain rate effect on the strength and crack initiation in the single-flawed specimen. In the theoretical study, the definition of the sign system is different from that in the numerical study. If the strain is tensile, the tensile stress and the corresponding strain rate is negative, contrary to the compressive stress and strain rate. For the micro-element method, the region around the flaw is divided into many virtual elements to evaluate localized stress, strain, strain rate and rate-dependent strength. The strain rate of a micro-element around the flaw $\dot{\varepsilon}_{pb}$ defined by the tangential strain variation over time can be obtained by dividing the derivative of tangential stress by the material elastic modulus E, assuming that the E is constant, as shown in Eq. (9). Previous experimental results show that the variation of the dynamic elastic modulus can be neglected in such a strain rate range (10–500 s^{-1}), and this assumption is reasonable.[19,67]

The present analysis has another assumption that the plastic deformation before the peak strength can be neglected, which is acceptable in dynamic tests for brittle materials. The typical stress-strain curve for a brittle rock is shown in Fig. 1. The quasi-linear elastic deformation dominates the loading period. Unlike the quasi-static loading conditions, the pre-peak plastic deformation is not obvious.

The element strain rate around the flaw $\dot{\varepsilon}_{pb}$ is given by Eq. (9).

$$\dot{\varepsilon}_{pb} = \frac{\dot{\sigma}_b}{E} = \frac{\dot{\sigma}_b}{\dot{\sigma}_1} \bullet \frac{\dot{\sigma}_1}{E} = \frac{\dot{\sigma}_b}{\dot{\sigma}_1} \dot{\varepsilon}_1 \qquad \text{Eq. 9}$$

Based on the fitting curves of dynamic strength of different rocks from literatures, the increase of dynamic strength is depicted as the common logarithm of strain rate for both the uniaxial compressive and tensile strength.[19,32,45,52–62,68] The dynamic increase factors (DIF) for compressive strength (CDIF) and tensile strength (TDIF) are then expressed by the following equations:

$$CDIF = A_c + B_c \, lg \, \dot{\varepsilon}_{pb} \, in \, dynamic \, regime \, m_c \le \dot{\varepsilon}_{pb} \le n_c \, CDIF$$
$$= C_c + D_c \, lg \, \dot{\varepsilon}_{pb} \, in \, quasi-static \, regime \, \dot{\varepsilon}_{pb} < m_c \qquad \text{Eq. 10}$$

(a)

(b)

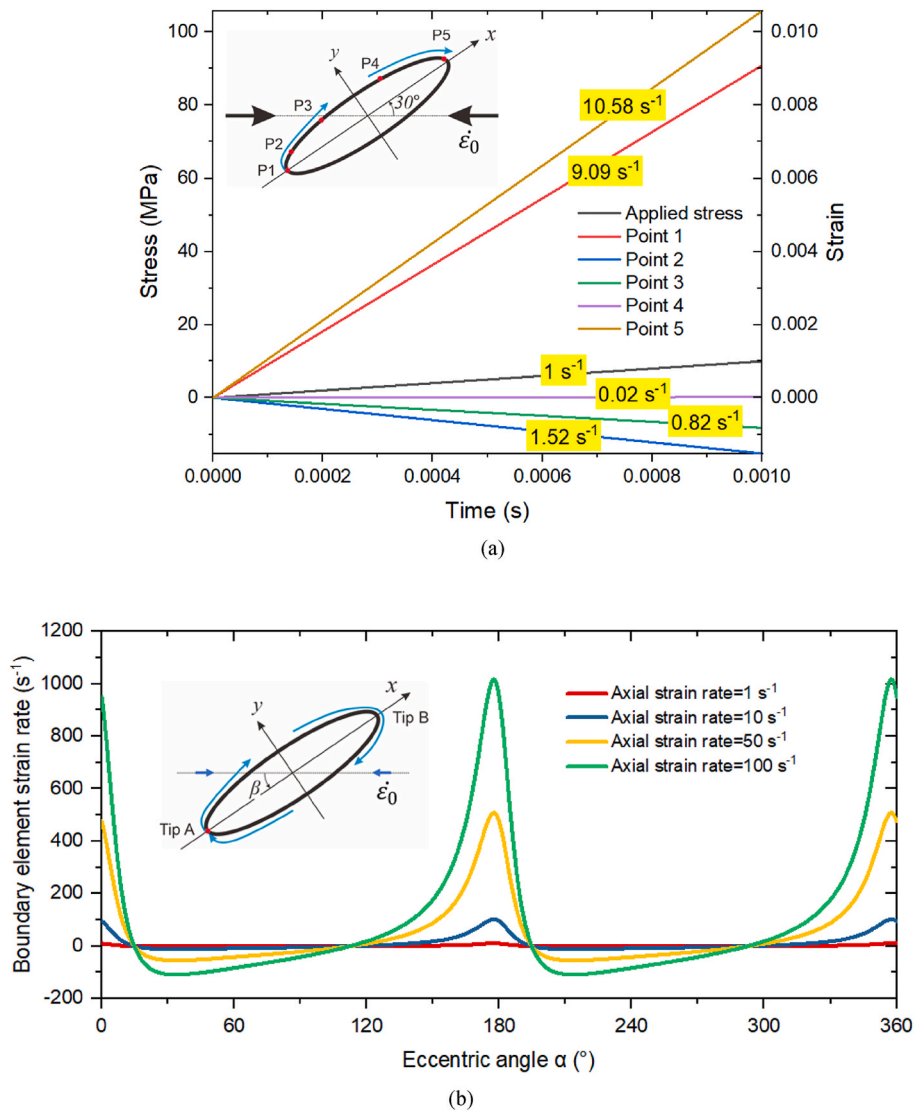**Fig. 11.** (1) Variation of stress and strain of five points along the flaw boundary undergoing linearly-increasing stress and the corresponding axial strain rate ($\dot{\varepsilon}_0 = 1$ s^{-1}). (2) Variation of the strain rate along the flaw boundary undergoing different axial strain rates $\dot{\varepsilon}_0$
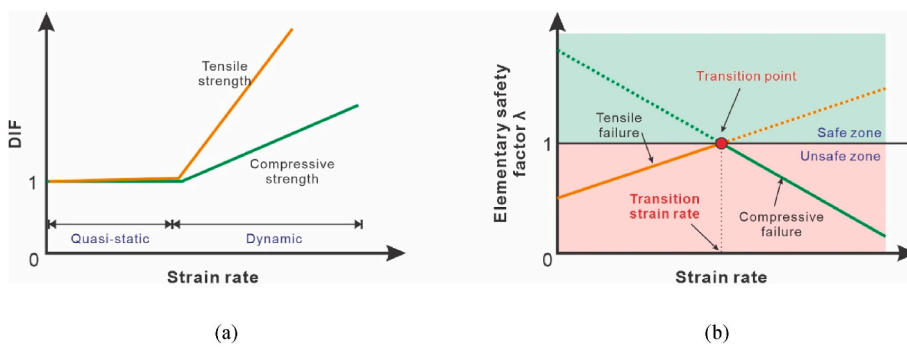

(a)

(b)

Fig. 12. Concept of transition strain rate and the elementary safety factor.
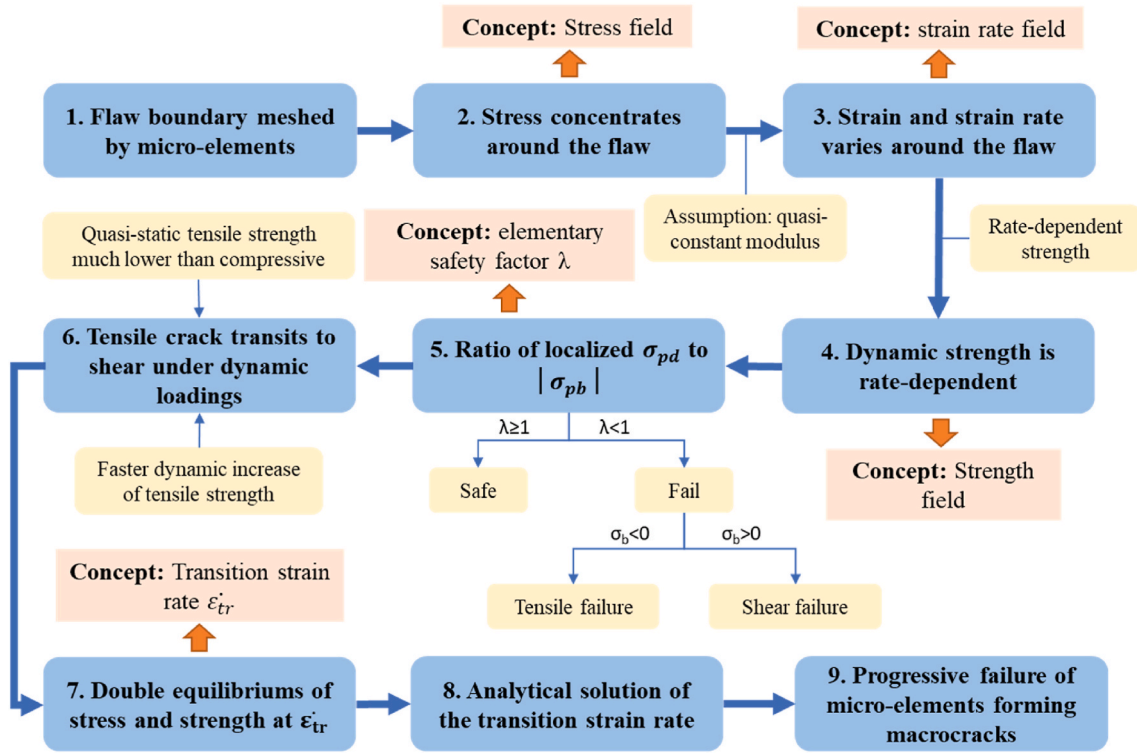
Fig. 13. Illustration of the micro-element method in analyzing the stress, strain, strain rate and strength around the flaw, as well as the corresponding concepts about stress field, strain rate field, rate-dependent strength field, elementary safety factor and the transition strain rate.

$$TDIF = A_t + B_t \lg \dot{\varepsilon}_{pb} \, in \, dynamic \, regime \, m_t \leq \dot{\varepsilon}_{pb} \leq n_t \, TDIF$$
$$= C_t + D_t \lg \dot{\varepsilon}_{pb} \, in \, quasi-staci \, regime \, \dot{\varepsilon}_{pb} < m_t \qquad \text{Eq. 11}$$

where A_c, B_c, C_c, D_c, A_t, B_t, C_t and D_t are the coefficients for CDIF and TDIF, respectively; m_c, n_c, m_t and n_t are the lower and upper limits. Combining Eq. (9), Eq. (10) and Eq. (11), the dynamic tensile strength σ_{dt} and the dynamic compressive strength σ_{dc} can be expressed by the following equations.

$$\sigma_{dt} = TDIF \bullet \sigma_t = \left(A_t + B_t \, log|\dot{\varepsilon}_{pb}|\right) \bullet \sigma_t, \text{for } m_t \leq |\dot{\varepsilon}_{pb}| \leq n_t \qquad \text{Eq. 12}$$

$$\sigma_{dc} = CDIF \bullet \sigma_c = \left(A_c + B_c \, log \, \dot{\varepsilon}_{pb}\right) \bullet \sigma_c, \text{for } m_c \leq \dot{\varepsilon}_{pb} \leq n_c \qquad \text{Eq. 13}$$

For the uniaxial compression tests ($\sigma_2 = 0$, and $\sigma_3 = 0$), we obtain that

$$\sigma_x = \frac{\sigma_1}{2} + \frac{\sigma_1}{2} \bullet \cos 2\beta \qquad \text{Eq. 14}$$

$$\sigma_y = \frac{\sigma_1}{2} - \frac{\sigma_1}{2} \bullet \cos 2\beta \qquad \text{Eq. 15}$$

$$\tau_{xy} = \frac{\sigma_1}{2} \bullet \sin 2\beta \qquad \text{Eq. 16}$$

Based on Eq. (3), the tangential stress on the boundary of the ellipse σ_b becomes

$$\sigma_b = \frac{\sigma_1}{m^2 cos^2 \alpha + sin^2 \alpha} \left\{ \left(\frac{1}{2} + \frac{1}{2} \bullet \cos 2\beta\right) \left[m(m+2)cos^2 \alpha - sin^2 \alpha\right] + \left(\frac{1}{2} - \frac{1}{2}\right. \right.$$
$$\left. \bullet \cos 2\beta\right) \left[(1+2m)sin^2 \alpha - m^2 cos^2 \alpha\right] - (1+m^2)\sin 2\beta \sin \alpha \cos \alpha \right\}$$
$$= M(\alpha, \beta, m)\sigma_1$$
$$\text{Eq. 17}$$

Substituting Eq. (17) into Eq. (9) gives:

$$\dot{\varepsilon}_{pb} = \frac{\dot{\sigma}_b}{\dot{\sigma}_1}\dot{\varepsilon}_1 = \frac{\dot{\varepsilon}_1}{m^2 cos^2 \alpha + sin^2 \alpha} \left\{ \left(\frac{1}{2} + \frac{1}{2} \bullet \cos 2\beta\right) \left[m(m+2)cos^2 \alpha - sin^2 \alpha\right] + \left(\frac{1}{2} - \frac{1}{2}\right. \right.$$
$$\left. \bullet \cos 2\beta\right) \left[(1+2m)sin^2 \alpha - m^2 cos^2 \alpha\right] - (1+m^2)\sin 2\beta \sin \alpha \cos \alpha \right\} = M(\alpha, \beta, m)\dot{\varepsilon}_1 \qquad \text{Eq. 18}$$

According to the definition of sign of stress, positive $\dot{\varepsilon}_{pb}$ represents the compressive strain rate, while negative $\dot{\varepsilon}_{pb}$ represents the tensile strain rate.

Under dynamic loadings with the element strain rate $\dot{\varepsilon}_{pb}$, the crack initiation is determined by the ratio of tangential stress to strength. Along the flaw boundary, when $\frac{\sigma_{t-max}}{\sigma_{t-dyn}} > 1$ and $\frac{\sigma_{c-max}}{\sigma_{c-dyn}} > 1$, the tensile crack will initiate. On the contrary, the compressive crack or the shear crack will initiate.
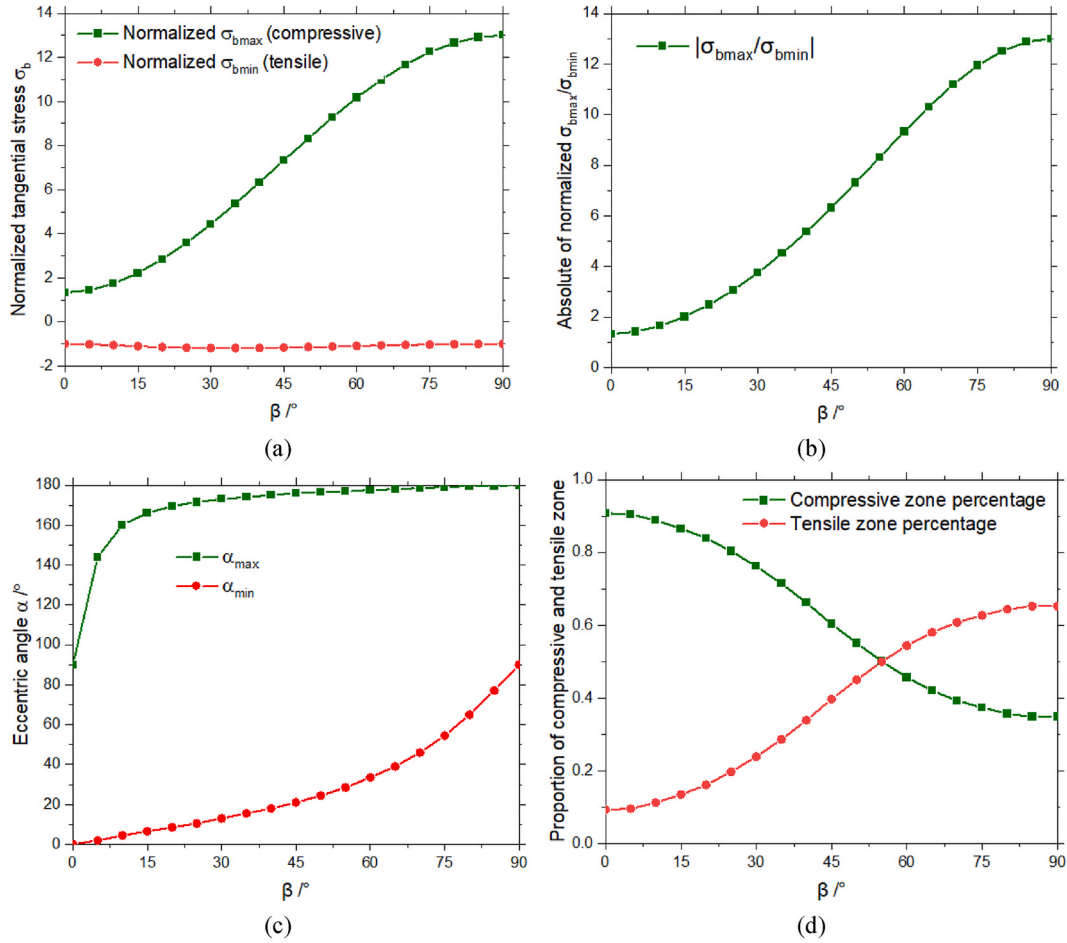
Fig. 14. Variation of the normalized tangential stress (a), ratio of the max/min tangential stress (b), the eccentric angle corresponding to the max and min tangential stress (c) and the proportion of compressive and tensile zones (d) with the flaw inclination angle β as defined by Fig. 7.

5. Transition strain rate

For the single-flawed specimen, the transition strain rate $\dot{\varepsilon}_{tr}$ is defined as the strain rate corresponding to the inflection point of the first crack mode initiated along the flaw boundary from tensile to compressive (shear). It is necessary to differentiate the element strain rate and the applied strain rate: the former is the local strain rate of each micro-element. At the same time, the latter is the strain rate of the applied force on the specimen boundaries, which can be considered the average strain rate of the whole specimen. The transition strain rate belongs to the applied strain rate. When the applied strain rate of the specimen is higher than the transition strain rate, the initiation mode, initiation position, failure mode and propagation of the first crack will be significantly different from those under quasi-static loadings.

When the element along the flaw boundary of the single-flawed specimen reaches the transition strain rate, the dynamic tangential stress equals the strength for both the compressive and tensile failure modes. In the compression zone ($\sigma_b \geq 0$ or $M(\alpha, \beta, m) \geq 0$) with the dynamic strain rate range $m_c \leq \dot{\varepsilon}_{pb} \leq n_c$, the maximum tangential stress under uniaxial compression ($\sigma_1 > 0$, $\sigma_3 = 0$, and $\sigma_2 = 0$),

$$\sigma_{bmax} = \sigma_{dc} \qquad \text{Eq. 19}$$

$$M(\alpha_{max}, \beta, m)\sigma_1 = \left(A_c + B_c \, lg \, \dot{\varepsilon}_{pb}\right)\sigma_c = [A_c + B_c \, lg(M(\alpha_{max}, \beta, m)\dot{\varepsilon}_{tr})]\sigma_c \qquad \text{Eq. 20}$$

At this moment, the absolute value of the minimum tangential stress (tensile and negative) should equal the corresponding dynamic tensile strength.
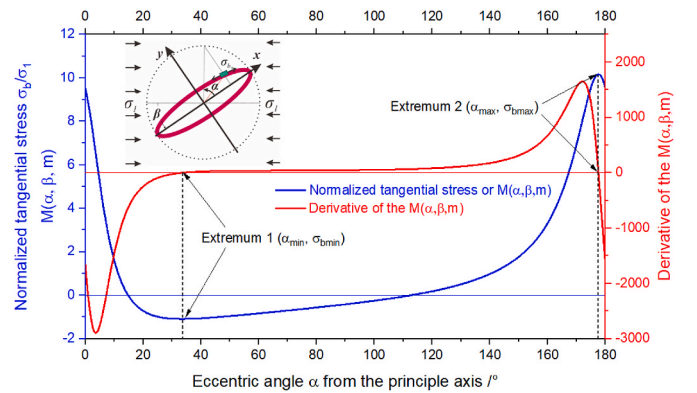

Fig. 15. Normalized tangential stress along the elliptical flaw boundary regarding the eccentric angle from the principal axis for the single-flawed specimen with the inclination angle of 60°[65].

$$|\sigma_{bmin}| = \sigma_{dt} \qquad \text{Eq. 21}$$

$$-M(\alpha_{min}, \beta, m)\sigma_1 = \left(A_t + B_t \, lg|\dot{\varepsilon}_{pb}|\right)\sigma_t = [A_t + B_t \, lg(-M(\alpha_{min}, \beta, m)\dot{\varepsilon}_{tr})]\sigma_t \qquad \text{Eq. 22}$$

where α_{max} and α_{min} are the eccentric angles corresponding to the positions of the failure element for the maximum and minimum tangential stresses.

Table 2
Equations of the transition strain rate for specimens with different inclination angles.

$\beta/°$	Equation for transition strain rate	α_{min}	M_{min}	α_{max}	M_{max}	$\dot\epsilon_{cr}$
0	$\dot\epsilon_{cr} = \left(\dfrac{1.00^{1.33Bt\bullet\frac{\sigma_t}{\sigma_c}} \times 10^{1.33At\bullet\frac{\sigma_t}{\sigma_c}} - Ac}{1.33^{Bc}}\right)^{1/\left(Bc-1.33Bt\bullet\frac{\sigma_t}{\sigma_c}\right)}$	0	−1.0	90.0	1.3	0.5
15	$\dot\epsilon_{cr} = \left(\dfrac{1.10^{2.01Bt\bullet\frac{\sigma_t}{\sigma_c}} \times 10^{2.01At\bullet\frac{\sigma_t}{\sigma_c}} - Ac}{2.22^{Bc}}\right)^{1/\left(Bc-2.01Bt\bullet\frac{\sigma_t}{\sigma_c}\right)}$	6.4	−1.1	166.1	2.2	0.5
30	$\dot\epsilon_{cr} = \left(\dfrac{1.19^{3.74Bt\bullet\frac{\sigma_t}{\sigma_c}} \times 10^{3.74At\bullet\frac{\sigma_t}{\sigma_c}} - Ac}{4.44^{Bc}}\right)^{1/\left(Bc-3.74Bt\bullet\frac{\sigma_t}{\sigma_c}\right)}$	13.0	−1.2	173.1	4.4	0.5
45	$\dot\epsilon_{cr} = \left(\dfrac{1.16^{6.31Bt\bullet\frac{\sigma_t}{\sigma_c}} \times 10^{6.31At\bullet\frac{\sigma_t}{\sigma_c}} - Ac}{7.33^{Bc}}\right)^{1/\left(Bc-6.31Bt\bullet\frac{\sigma_t}{\sigma_c}\right)}$	21.2	−1.2	175.9	7.3	0.5
60	$\dot\epsilon_{cr} = \left(\dfrac{2.24^{9.33Bt\bullet\frac{\sigma_t}{\sigma_c}} \times 10^{9.33At\bullet\frac{\sigma_t}{\sigma_c}} - Ac}{10.17^{Bc}}\right)^{1/\left(Bc-9.33Bt\bullet\frac{\sigma_t}{\sigma_c}\right)}$	33.5	−1.1	177.6	10.2	5.95
75	$\dot\epsilon_{cr} = \left(\dfrac{1.03^{11.94Bt\bullet\frac{\sigma_t}{\sigma_c}} \times 10^{11.94At\bullet\frac{\sigma_t}{\sigma_c}} - Ac}{12.24^{Bc}}\right)^{1/\left(Bc-11.94Bt\bullet\frac{\sigma_t}{\sigma_c}\right)}$	54.7	−1.0	178.9	12.2	2.2
90	$\dot\epsilon_{cr} = \left(\dfrac{1.00^{13Bt\bullet\frac{\sigma_t}{\sigma_c}} \times 10^{13At\bullet\frac{\sigma_t}{\sigma_c}} - Ac}{13.00^{Bc}}\right)^{1/\left(Bc-13Bt\bullet\frac{\sigma_t}{\sigma_c}\right)}$	90	−1.0	180	13.0	1.77

Divide Eq. (20) by Eq. (22), the $\dot\epsilon_{tr}$ becomes the only unknown variant except for these coefficients for the material properties:

$$\frac{M(\alpha_{max},\beta,m)}{-M(\alpha_{min},\beta,m)} = \frac{A_c + B_c\,lg(M(\alpha_{max},\beta,m)\dot\epsilon_{tr})}{A_t + B_t\,lg(-M(\alpha_{min},\beta,m)\dot\epsilon_{tr})} \times \frac{\sigma_c}{\sigma_t} \qquad \text{Eq. 23}$$

Therefore, the transition strain rate $\dot\epsilon_{cr}$ is finally given by the following equation.

$$\dot\epsilon_{tr} = \left[\frac{(-M(\alpha_{min},\beta,m))^{\frac{B_t M(\alpha_{max},\beta,m)\sigma_t}{-M(\alpha_{min},\beta,m)\sigma_c}} \times 10^{\frac{A_t M(\alpha_{max},\beta,m)\sigma_t}{-M(\alpha_{min},\beta,m)\sigma_c} - A_c}}{M(\alpha_{max},\beta,m)^{B_c}}\right]^{\frac{1}{B_c - \frac{B_t M(\alpha_{max},\beta,m)\sigma_t}{-M(\alpha_{min},\beta,m)\sigma_c}}} \qquad \text{Eq. 24}$$

This equation is for general conditions. The equation can be simplified and more practical for specimens with a specific single flaw,

α_{min} and α_{max}.

In order to obtain the value of the eccentric angles α_{min} and α_{max}, the derivative of the $M(\alpha,\beta,m)$ equal to zero is solved, as shown in Eq. (25). Substituting the value of β and m by 60 and 1/6 gets Eq. (26). However, it is an implicit equation. The explicit equation based on the analytical solution is hard to obtain. A numeric solution by MATLAB coding is used to solve this equation. The solutions of the eccentric angles α_{min} and α_{max} are 33.5° and 177.6°, while the corresponding values of the $M(\alpha_{min},\beta,m)$ and $M(\alpha_{max},\beta,m)$ are determined as −1.09 and 10.17, respectively.

$$\frac{\partial M(\alpha,\beta,m)}{\partial\alpha} = \frac{\partial M(\alpha,60,1/6)}{\partial\alpha} = 0 \qquad \text{Eq. 25}$$

where α varies from 0 to 180°.

$$\frac{35\cos\alpha\sin\alpha\bullet\left(\frac{65\sin^2\alpha}{3} - \frac{247\cos^2\alpha}{18} + \frac{481\sqrt{3}\cos\alpha\sin\alpha}{18}\right)}{18\bullet\left(\frac{\cos^2\alpha}{36} + \sin^2\alpha\right)^2} - \frac{\frac{637\cos\alpha\sin\alpha}{9} - \frac{481\sqrt{3}\sin^2\alpha}{18} + \frac{481\sqrt{3}\cos^2\alpha}{18}}{\frac{\cos^2\alpha}{36} + \sin^2\alpha} = 0 \qquad \text{Eq. 26}$$

as stated in the following sections.

5.1. Single-flaw with 60° inclination angle

In this section, the transition strain rate equation for a single-flawed specimen with a 60° flaw inclination angle is derived. The equations for other inclination angles are given in the next section. The specimen under uniaxial compression contains an elliptical flaw with a 60° inclination angle ($\beta = 60°$) and the flatness $m = 1/6$. With these values of inclination angle and flaw flatness, the variation of σ_b regarding the eccentric angle α under uniaxial compression stress σ_1 can be obtained by Eq. (17) and illustrated in Fig. 15. The tangential stress is normalized for better illustration by being divided by σ_1. According to Eq. (17), the normalized tangential stress equals the function $M(\alpha,\beta,m)$. The two extrema σ_{bmin} and σ_{bmax} in Fig. 15 represent the maximum tensile stress which is negative and the maximum compressive stress which is positive, respectively. The corresponding eccentric angles are marked by

Substituting the values of α_{min} and α_{max} to Eq. (24), the $\dot\epsilon_{tr}$ is then obtained, as illustrated by Eq. (27). Specimens with an applied strain rate higher than $\dot\epsilon_{tr}$ will change the failure mode from tensile to compressive or shear if the original failure mode is tensile for a rock.

$$\dot\epsilon_{cr} = \left(\frac{2.24^{9.33Bt\bullet\frac{\sigma_t}{\sigma_c}} \times 10^{9.33At\bullet\frac{\sigma_t}{\sigma_c}} - Ac}{10.17^{Bc}}\right)^{1/\left(Bc-9.33Bt\bullet\frac{\sigma_t}{\sigma_c}\right)} \qquad \text{Eq. 27}$$

5.2. Single-flaw with other inclination angles

Similar solution processes to section 5.1 are conducted for the single-flawed specimens with inclination angles from 0° to 90° with an interval of 15°. For the same flatness m of 1/6, the equations of the transition strain rate are listed in Table 2, which also provides the normalized
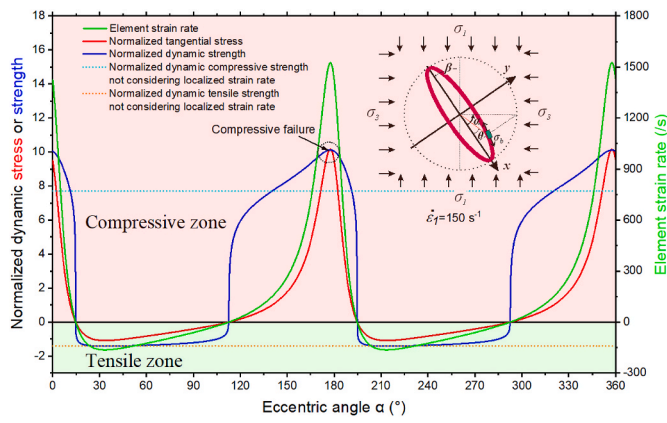
Fig. 16. Tangential stress, strain rate and the corresponding strength of the micro-elements along the flaw boundary for Carrara marble ($\beta = 60°$) under dynamic loadings.

values of the maximum and minimum tangential stress as well as the corresponding eccentric angles.

5.3. Transition strain rate of single-flawed carrara marble

As determined by the experiments, the CDIF and TDIF of the Carrara marble versus strain rate have the forms shown in Eq. (1) and Eq. (2). The average quasi-static uniaxial compressive strength and tensile strength of the Carrara marble are 90 MPa and 6.86 MPa, respectively. The coefficients A_c, B_c, A_t, and B_t for the marble are determined to be 1.426, 1.390, 2.414 and 3.784 in the dynamic regime ($0.5\ s^{-1} \le |\dot{\varepsilon}_{pb}|$). According to the equations given in Table 2, the transition strain rate of Carrara marble specimens with different flaw inclination angles can be calculated. For those transition strain rates less than $0.5\ s^{-1}$, the result is revised to be $0.5\ s^{-1}$ because the equation is only valid in the dynamic regime. The results are also given in Table 2.

6. Discussion

6.1. Dynamic strain rate and strength along the flaw boundary

The variation of tangential stress, strain rate and the corresponding strength of the micro-elements along the flaw boundary ($\beta = 60°$) in the Carrara marble is illustrated in Fig. 16. The applied strain rate is $150\ s^{-1}$, much higher than the transition strain rate. Normalized tangential stress and the strength of these micro-elements are calculated to show the comparison between them. Two cases are designed to evaluate the importance of considering the strain rate field and the rate-dependent strength field in rock dynamics: (1) Case A - strain rate field not considered; (2) Case B - strain rate field considered. This case study will help understand the concept of strain rate and rate-dependent strength fields in flawed rock. From Fig. 16, it is found that the maximum dynamic strengths for both compressive and tensile modes in Case B are larger than the dynamic strength in Case A.

(1) Case A - strain rate field NOT considered

In this case, the strain rate of the micro-elements along the flaw boundary is constant and equal to $150\ s^{-1}$. Hence, the dynamic compressive and tensile strengths of these micro-elements are invariant with a value of 90 MPa and 6.86 MPa, respectively. As shown in Fig. 17, since the tensile strength is much lower than the compressive strength, tensile failure occurs first, which contradicts the experimental phenomenon. All the stresses and rate-dependent strengths are normalized by being divided by the uniaxial stress σ_1.
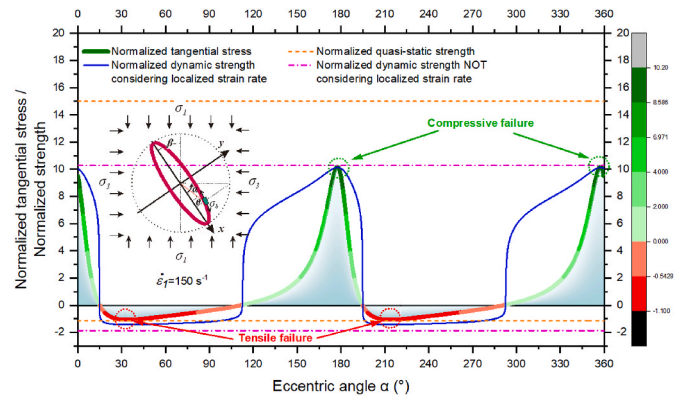

Fig. 17. Change of failure mode based on (1) quasi-static strength, (2) dynamic strength NOT considering localized strain rate, and (3) dynamic strength considering localized strain rate along the flaw boundary for Carrara marble ($\beta = 60°$) under dynamic loadings (applied strain rate 150 s^{-1}).

(2) Case B - strain rate field considered

When the strain rate field or the localized strain rate effect is considered, the strength of the micro-elements will not be equal again but vary with the positions. The localized strain rate changes the micro-element strength. Then, the normalized tangential stress and the normalized strength vary with the eccentric angle. In Fig. 17, the dynamic compressive stress will first reach the dynamic compressive strength and lead to the compressive failure mode. The crack initiation point and the crack type are all changed. The compressive or shear crack will initiate first.

This case study indicates that the influence of strain rate on strength must be considered in high strain rate loading. Otherwise, inferences about the cracking behaviour will become unreliable.

6.2. Dynamic failure mode

In the SHPB tests, the single-flawed marble generally fails with an X-shaped crack pattern. The previous analysis only interprets the suppression of tensile cracks and the change of first cracks to shear cracks. According to Fig. 17, the maximum normalized tensile stress is also close to the corresponding strength when the normalized compressive stress reaches the strength. Because of the limited crack propagation speed, the tensile failure will also be achieved in a very short time. Therefore, it looks like these two groups of cracks initiate simultaneously and forms the X-shaped failure pattern.

6.3. Inertia effect

The inertia effect can be neglected compared with other influencing factors in SHPB tests and is therefore not considered in the present study, though the inertia effect is inevitable in dynamic problems. The inertia force depends on the acceleration at the corresponding direction. Several theories and equations have been given to calculate the inertia stress applied on the specimen in the SHPB tests.[69] Samanta (1971) proposed a corrected equation to calculate the actual dynamic stress on the specimens in SHPB tests.[70] From this equation, when the specimen length-to-diameter ratio is close to $\sqrt{3}/4$ and the strain rate is constant, the inertia force or stress can be eliminated. Gorham (1989) and Forrestal et al. (2006) also provided the explicit expression of the inertia stress.[71,72] According to these equations, it is found that the inertia stress has an amplitude of about 1 MPa or below for specimens without large plastic deformations. In other words, for brittle rocks or most engineering rocks, the contribution of the inertia stress to the dynamic strength can be negligible because of the normal dynamic strength as a value about 100–1000 MPa. The influence of the inertia effect on the

total dynamic stress is less than 1%.

7. Conclusions

"Localized strain rate effect" depicting the uneven distribution of deformation and strain rate around a flaw in rock is the key point of the present research. The localized distribution of the rate-dependent strength of flawed rock is prominent under dynamic loadings, under which rock strength is sensitive to the strain rates. For materials with defects or flaws, this uneven strain rate and rate-dependent strength distribution should be considered in crack initiation. Thus, the concepts of the strain rate field and strength field are proposed. The cracking behaviours under dynamic and quasi-static loadings are significantly different. The present study establishes the connection between the rate-dependent strength and rock cracking behaviour and explains why tensile cracks are commonly suppressed under dynamic loadings. With the experimental rate-dependent strength, the mathematical expression of the transition strain rate is obtained by an analytical solution, which theoretically explains the experimental phenomenon. The findings can provide some interpretations for high strain rate-related earth science problems, like earthquakes, volcano eruptions and meteorite impacts. Further experimental and numerical investigations on other types of mechanical properties and their influences on fracturing are warranted.

Declaration of competing interest

The authors declare that they have no known competing financial interests or personal relationships that could have appeared to influence the work reported in this paper.

Data availability

Data will be made available on request.

Acknowledgements

References

1 Ma G, Hao H, Wang F. Simulations of explosion-induced damage to underground rock chambers. *J Rock Mech Geotech Eng.* 2011;3(1):19–29.

2 Turcotte DL. Fractals and fragmentation. *J Geophys Res Solid Earth.* 1986;91(B2): 1921–1926.

3 Melosh HJ, Ryan EV, Asphaug E. Dynamic fragmentation in impacts: hydrocode simulation of laboratory impacts. *J Geophys Res: Planets.* 1992;97(E9):14735–14759.

4 Levitas VI, Ravelo R. Virtual melting as a new mechanism of stress relaxation under high strain rate loading. *Proc Natl Acad Sci USA.* 2012;109(33), 13204.

5 Fredrich JT, Evans B, Wong T-F. Micromechanics of the brittle to plastic transition in Carrara marble. *J Geophys Res Solid Earth.* 1989;94(B4):4129–4145.

6 Brace WF, Bombolakis EG. A note on brittle crack growth in compression. *J Geophys Res.* 1963;68(12):3709–3713.

7 Lajtai EZ. Brittle fracture in compression. *Int J Fract.* 1974;10(4):525–536.

8 Hoek E, Bieniawski ZT. Brittle fracture propagation in rock under compression. *Int J Fract.* 1984;26(4):276–294.

9 Einstein HH, Stephansson O. Fracture systems, fracture propagation and coalescence. In: *Geoeng2000-An International Conference on Geotechnical & Geological Engineering.* Melbourne, Australia: International Society for Rock Mechanics; 2000:1–41.

10 Wong LNY, Einstein HH. Systematic evaluation of cracking behavior in specimens containing single flaws under uniaxial compression. *Int J Rock Mech Min Sci.* 2009;46 (Compendex):239–249.

11 Atkinson BK. Subcritical crack growth in geological materials. *J Geophys Res Solid Earth.* 1984;89(B6):4077–4114.

12 Bobet A, Einstein HH. Fracture coalescence in rock-type materials under uniaxial and biaxial compression. *Int J Rock Mech Min Sci.* 1998;35(7):863–888.

13 Yang S-Q, Huang Y-H, Tian W-L, Zhu J-B. An experimental investigation on strength, deformation and crack evolution behavior of sandstone containing two oval flaws under uniaxial compression. *Eng Geol.* 2017;217(C):35–48.

14 Zou C, Maruvanchery V, Zhao X, He L. Change of crack mode in rock cracking process under quasi-static and dynamic loadings. *Geomechanics and Geophysics for Geo-Energy and Geo-Resources.* 2021;8(1):20.

15 Hazzard JF, Young RP, Maxwell SC. Micromechanical modeling of cracking and failure in brittle rocks. *J Geophys Res Solid Earth.* 2000;105(B7):16683–16697.

16 Li D, Han Z, Sun X, Zhou T, Li X. Dynamic mechanical properties and fracturing behavior of marble specimens containing single and double flaws in SHPB tests. *Rock Mech Rock Eng.* 2019;52(6):1623–1643.

17 Li X, Zhou T, Li D. Dynamic strength and fracturing behavior of single-flawed prismatic marble specimens under impact loading with a split-hopkinson pressure bar. *Rock Mech Rock Eng.* 2017;50(1):29–44.

18 Zou C, Wong LNY, Loo JJ, Gan BS. Different mechanical and cracking behaviors of single-flawed brittle gypsum specimens under dynamic and quasi-static loadings. *Eng Geol.* 2016;201:71–84.

19 Zou C, Wong LNY. Size and geometry effects on the mechanical properties of carrara marble under dynamic loadings. *Rock Mech Rock Eng.* 2016;49(5):1695–1708.

20 Zou C, Wong LNY. Experimental studies on cracking processes and failure in marble under dynamic loading. *Eng Geol.* 2014;173:19–31, 0.

21 Grady DE, Kipp ME. Dynamic rock fragmentation. In: Atkinson B, ed. *Fracture Mechanics of Rocks.* NY: Academic Press; 1987.

22 Meyers MA. *Dynamic Behavior of Materials/Marc A. Meyers.* New York ; Singapore: John Wiley & Sons, Inc.; 1994, 1994.

23 Bearman R, Briggs C, Kojovic T. The applications of rock mechanics parameters to the prediction of comminution behaviour. *Miner Eng.* 1997;10(3):255–264.

24 Banthia N, Mindess S, Bentur A, Pigeon M. Impact testing of concrete using a drop-weight impact machine. *Exp Mech.* 1989;29(1):63–69.

25 Grady DE, Kipp ME. The micromechanics of impact fracture of rock. *Int J Rock Mech Min Sci Geomech Abstracts.* 1979;16(5):293–302.

26 Zhao J, Zhou YX, Hefny AM, et al. Rock dynamics research related to cavern development for ammunition storage. *Tunn Undergr Space Technol.* 1999;14(4): 513–526.

27 Davies EDH, Hunter SC. The dynamic compression testing of solids by the method of the split Hopkinson pressure bar. *J Mech Phys Solid.* 1963;11(3):155–179.

28 Frew D, Forrestal M, Chen W. A split Hopkinson pressure bar technique to determine compressive stress-strain data for rock materials. *Exp Mech.* 2001;41(1):40–46.

29 Lok TS, Li XB, Liu D, Zhao PJ. Testing and response of large diameter brittle materials subjected to high strain rate. *J Mater Civ Eng.* 2002;14(3):262–269.

30 Zhao J. An overview of some recent progress in rock dynamics research. In: Zhou Y, Zhao J, eds. *Advances in Rock Dynamics and Applications.* CRC Press; 2011:5–33.

31 Dai F, Xia K, Zheng H, Wang YX. Determination of dynamic rock Mode-I fracture parameters using cracked chevron notched semi-circular bend specimen. *Eng Fract Mech.* 2011;78(15):2633–2644.

32 Li XB, Lok TS, Zhao J. Dynamic characteristics of granite subjected to intermediate loading rate. *Rock Mech Rock Eng.* 2005;38(1):21–39.

33 Kandula N, Cordonnier B, Boller E, Weiss J, Dysthe DK, Renard F. Dynamics of microscale precursors during brittle compressive failure in carrara marble. *J Geophys Res Solid Earth.* 2019;124(6):6121–6139.

34 Zou C, Li H. Combined numerical and experimental studies on the dynamic and quasi-static failure modes of brittle rock. *Int J Rock Mech Min Sci.* 2021;148, 104957.

35 Zou C, Cheng Y, Li J. Strain rate and size effects on the brittleness indexes of Carrara marble. In: *International Journal of Rock Mechanics and Mining Sciences.* 2021;146. Oxford, England : 1997.

36 Hashiba K, Okubo S, Fukui K. A new testing method for investigating the loading rate dependency of peak and residual rock strength. *Int J Rock Mech Min Sci.* 2006;43(6): 894–904.

37 Kawakami S-I, Mizutani H, Takagi Y, Kato M, Kumazawa M. Impact experiments on ice. *J Geophys Res Solid Earth.* 1983;88(B7):5806–5814.

38 Yamasaki T, Seno T. High strain rate zone in central Honshu resulting from the viscosity heterogeneities in the crust and mantle. *Earth Planet Sci Lett.* 2005;232 (1–2):13–27.

39 Wang Q, Li W, Song X. A method for testing dynamic tensile strength and elastic modulus of rock materials using SHPB. *Pure Appl Geophys.* 2006;163(5):1091–1100.

40 Zhao J, Li H. Experimental determination of dynamic tensile properties of a granite. *Int J Rock Mech Min Sci.* 2000;37(5):861–866.

41 Barbero M, Barla G, Zaninetti A. Dynamic shear strength of rock joints subjected to impulse loading. *Int J Rock Mech Min Sci.* 1996;33(2):141–151.

42 Kalthoff JF, Bürgel A. Influence of loading rate on shear fracture toughness for failure mode transition. *Int J Impact Eng.* 2004;30(8–9):957–971.

43 Zhang QB, Zhao J. Effect of loading rate on fracture toughness and failure micromechanisms in marble. *Eng Fract Mech.* 2013;102:288–309, 0.

44 Huang J, Chen G, Zhao Y, Wang R. An experimental study of the strain field development prior to failure of a marble plate under compression. *Tectonophysics.* 1990;175(1-3):269–284.

45 Wong LNY, Zou C, Cheng Y. Fracturing and failure behavior of carrara marble in quasistatic and dynamic Brazilian disc tests. *Rock Mech Rock Eng.* 2014;47(4): 1117–1133.

46 Ravichandran G, Subhash G. CRITICAL-APPRAISAL of limiting strain rates for compression testing of ceramics in a split HOPKINSON pressure bar. *J Am Ceram Soc.* 1994;77(1):263–267.

47 Zhang X, Ma L, Zhu Z, Zhou L, Wang M, Peng T. Experimental study on the energy evolution law during crack propagation of cracked rock mass under impact loads. *Theor Appl Fract Mech.* 2022;122, 103579.

48 Alneasan M, Behnia M. Strain rate effects on the crack propagation speed under different loading modes (I, II and I/II): experimental investigations. *Eng Fract Mech.* 2021;258, 108118.

49 Liu R, Zhu Z, Li Y, Liu B, Wan D, Li M. Study of rock dynamic fracture toughness and crack propagation parameters of four brittle materials under blasting. *Eng Fract Mech.* 2020;225, 106460.

50 Zhang QB, Zhao J. Effect of loading rate on fracture toughness and failure micromechanisms in marble. *Eng Fract Mech.* 2013;102:288–309.

51 Hao Y, Hao H. Numerical evaluation of the influence of aggregates on concrete compressive strength at high strain rate. *International Journal of Protective Structures.* 2011;2(2):177–206.

52 Cho SH, Ogata Y, Kaneko K. Strain-rate dependency of the dynamic tensile strength of rock. *Int J Rock Mech Min Sci.* 2003;40(5):763–777.

53 Ross CA, Thompson PY, Tedesco JW. Split-Hopkinson pressure-bar tests on concrete and mortar in tension and compression. *ACI Mater J.* 1989;86(5):475–481.

54 Klepaczko JR, Brara A. An experimental method for dynamic tensile testing of concrete by spalling. *Int J Impact Eng.* 2001;25(4):387–409.

55 Grote DL, Park SW, Zhou M. Dynamic behavior of concrete at high strain rates and pressures: I. experimental characterization. *Int J Impact Eng.* 2001;25(9):869–886.

56 Cai M, Kaiser P, Suorineni F, Su K. A study on the dynamic behavior of the Meuse/ Haute-Marne argillite. *Phys Chem Earth, Parts A/B/C.* 2007;32(8):907–916.

57 Li Y, Xia C. Time-dependent tests on intact rocks in uniaxial compression. *Int J Rock Mech Min Sci.* 2000;37(3):467–475.

58 Sylven ET, Agarwal S, Briant CL, Cleveland RO. High strain rate testing of kidney stones. *J Mater Sci Mater Med.* 2004;15(5):613–617.

59 Lindholm U, Yeakley L, Nagy A. The dynamic strength and fracture properties of dresser basalt. *Int J Rock Mech Min Sci Geomech Abstracts.* 1974;11(5):181–191.

60 Xia K, Nasseri MHB, Mohanty B, Lu F, Chen R, Luo SN. Effects of microstructures on dynamic compression of Barre granite. *Int J Rock Mech Min Sci.* 2008;45(6):879–887.

61 Goldsmith W, Sackman J, Ewerts C. Static and dynamic fracture strength of Barre granite. *Int J Rock Mech Min Sci Geomech Abstracts.* 1976;13(11):303–309.

62 Olsson W. The compressive strength of tuff as a function of strain rate from 10<sup>− 6 to 10< sup> 3/sec. *Int J Rock Mech Min Sci Geomech Abstracts.* 1991;28(1): 115–118.

63 Wong NY. *Crack Coalescence in Molded Gypsum and Carrara Marble. Department of Civil and Environmental Engineering.* PhD. Massachusetts Institute of Technology; 2008:876.

64 Hoek E. Brittle failure of rock. In: Stagg KG, Zienkiewicz OC, eds. *Rock Mechanics in Engineering Practice.* London: Wiley; 1968:99–124.

65 Zou C, Li J, Zhao X, Zhao J. Why are tensile cracks suppressed under dynamic loading?—transition strain rate for failure mode. *Extreme Mech Lett.* 2021, 101506.

66 Wong LNY, Einstein HH. Crack coalescence in molded gypsum and carrara marble: Part 1. macroscopic observations and interpretation. *Rock Mech Rock Eng.* 2009;42 (Compendex):475–511.

67 Zhao J, Li HB, Wu MB, Li TJ. Dynamic uniaxial compression tests on a granite. *Int J Rock Mech Min Sci.* 1999;36(2):273–277.

68 Zhao J. Applicability of Mohr–Coulomb and Hoek–Brown strength criteria to the dynamic strength of brittle rock. *Int J Rock Mech Min Sci.* 2000;37(7):1115–1121.

69 Chen WW. *Split Hopkinson (Kolsky) Bar Design, Testing and Applications.* New York: New York: Springer; 2011.

70 Samanta SK. Dynamic deformation of aluminium and copper at elevated temperatures. *J Mech Phys Solid.* 1971;19(3):117–135.

71 Gorham DA. Specimen inertia in high strain-rate compression. *J Phys D Appl Phys.* 1989;22(12):1888.

72 Forrestal MJ, Wright TW, Chen W. The effect of radial inertia on brittle samples during the split Hopkinson pressure bar test. *Int J Impact Eng.* 2007;34(3):405–411.

73 Liu K, Zhang QB, Zhao J. Dynamic increase factors of rock strength. In: *Rock Dynamics–Experiments, Theories and Applications.* CRC Press; 2018:169–174.